Naval Research Laboratory

Washington, DC 20375-5320

NRL/MR/6790--06-8974

SPARC - A Simulation Model for Electrical Discharges

D.F. GORDON
P. SPRANGLE
S. SLINKER

Beam Physics Branch
Plasma Physics Division

R. FERNSLER

Charged Particle Physics Branch
Plasma Physics Division

M. LAMPE

Plasma Physics Division

September 20, 2006

REPORT DOCUMENTATION PAGE

Form Approved
OMB No. 0704-0188

1. REPORT DATE *(DD-MM-YYYY)*
20-09-2006

2. REPORT TYPE
Interim Report

3. DATES COVERED *(From - To)*
August 2005 - August 2006

4. TITLE AND SUBTITLE
SPARC - A Simulation Model for Electrical Discharges

5a. CONTRACT NUMBER

5b. GRANT NUMBER

5c. PROGRAM ELEMENT NUMBER

6. AUTHOR(S)
D.F. Gordon, P. Sprangle, R. Fernsler, M. Lampe, and S. Slinker

5d. PROJECT NUMBER
67-8914-06

5e. TASK NUMBER

5f. WORK UNIT NUMBER

7. PERFORMING ORGANIZATION NAME(S) AND ADDRESS(ES)

Naval Research Laboratory
4555 Overlook Avenue, SW
Washington, DC 20375-5320

8. PERFORMING ORGANIZATION REPORT NUMBER
NRL/MR/6790--06-8974

9. SPONSORING / MONITORING AGENCY NAME(S) AND ADDRESS(ES)

Naval Sea Systems Command
1333 Isaac Hull Avenue, SE
Washington Navy Yard
Washington, DC 20376-5013

10. SPONSOR / MONITOR'S ACRONYM(S)
NAVSEA

11. SPONSOR / MONITOR'S REPORT NUMBER(S)

12. DISTRIBUTION / AVAILABILITY STATEMENT

Approved for public release; distribution is unlimited.

13. SUPPLEMENTARY NOTES

14. ABSTRACT

A simulation model for electrical discharges which is capable of modeling streamer and leader propagation over long distances is described. The model couples an electrostatic field solver, a chemistry package, and a package for solving the hydrodynamic equations for a multi-species plasma. Optionally, an implicit solution of the fluid equations for the electrons can be used to allow for long time steps. Due to the computationally demanding nature of the problem, the code features a semi-adaptive grid based on a sliding re-zone technique. The code is also parallelized and has been successfully scaled to hundreds of processors. Sample results are given showing streamer propagation over long distances, the streamer to leader transition, and hydrodynamic expansion of the hot gas.

15. SUBJECT TERMS

Simulation model	Streamer and leader propagation	Fluid equations
Electrical discharges	Hydrodynamic equations	

16. SECURITY CLASSIFICATION OF:

a. REPORT	b. ABSTRACT	c. THIS PAGE	17. LIMITATION OF ABSTRACT	18. NUMBER OF PAGES
Unclassified	Unclassified	Unclassified	UL	41

19a. NAME OF RESPONSIBLE PERSON
Daniel F. Gordon

19b. TELEPHONE NUMBER *(include area code)*
(202) 767-5036

Standard Form 298 (Rev. 8-98)
Prescribed by ANSI Std. Z39.18

Contents

I. INTRODUCTION

An electrical discharge is a complex phenomenon involving electrodynamics, hydrodynamics, radiation processes, and chemistry [1]. Over the years, substantial experimental, theoretical, and numerical research has been carried out in this area due to interest in natural lightning, plasma sources, and more recently, electrical discharges guided by femtosecond lasers [2, 3, 4, 5, 6]. Much of the numerical work has focused on streamer propagation, defined as the propagation of a filamentary ionization wave in a cold gas [7, 8, 9, 10, 11, 12, 13]. The approach typically used is to couple Poisson's equation to a continuity equation for electron, positive ion, and negative ion densities, and to solve these equations in two dimensional axisymmetric geometry. Air chemistry is usually reduced to three reactions: avalanche ionization, attachment, and recombination. A key assumption that is almost universally made is that the rate coefficients depend only on the parameter E/n_g, where E is the electric field and n_g is the neutral gas density. Although this is valid for a cold gas, it precludes accurately describing the leader phase in which the gas is hot enough to maintain the electron density even in low field regions. The code described in this report, SPARC (Streamer Propagation and ARCing), uses a more complete air chemistry model which is appropriate for either the streamer or leader phase. The code also includes hydrodynamics of the heavy species which might be important for long propagation distances in which there is enough time for the hot gas to expand.

Computer modeling of electrical discharges is difficult not only because of the complex physics involved, but also because of the problem of carrying out the calculation on a practical timescale. Streamers and leaders are characterized by a very short spatial scale (microns) at their extremity and a much longer spatial scale (meters) in their body. A similar disparity can exist in the temporal scales. For example, in the case of a laser induced discharge in air, the timescale for electrons to lose energy to Nitrogen vibrations is picoseconds, while the hydrodynamic timescale can be microseconds. For uniformly spaced grid cells and time levels, this implies that millions of cells and millions of time levels would be needed just to do a one-dimensional calculation. The solution adopted in this work is three fold. First, an adaptive grid is used so that tightly packed grid cells are only used where they are needed. Second, the code is written to take advantage of massively parallel computer architectures. Third, a heierarchy of models is introduced which allow various approximations to be in-

---

Manuscript approved August 16, 2006.

voked *optionally* at run-time. These approximations are designed to allow longer time steps to be taken while maintaining numerical stability.

The heierarchy of models contains several levels of approximation. At the highest level, the full hydrodynamic equations are solved for every species including the electrons. This requires resolving the plasma period and the electron collision time. At the next level of approximation, mobility limited flow is assumed. This requires resolving the charge redistribution time, but not the plasma period or electron collision time. At the next level of approximation, the electron motion is treated implicitly and quasineutrality is invoked in certain evaluations. In this case none of the detailed electron motion needs to be resolved. Instead, the minimum time step is determined by fast chemistry such as electron cooling. The fast chemistry can also be treated implicitly if desired. In every case, the heavy particles can be held fixed for further computational savings.

II. FULL ELECTROSTATIC-HYDRODYNAMIC MODEL

A. Basic Equations

For each species, define the density n_s, fluid velocity $\mathbf{v}_s$, energy density u_s, mass m_s, and charge q_s. It is assumed the translational and rotational modes are in thermal equilibrium, but the vibrational modes are not. The energy density is therefore written as

$$u_s = \frac{1}{2} n_s m_s v_s^2 + \Theta_s + \Xi_s \tag{1}$$

where Θ_s accounts for translational and rotational thermal energy, and Ξ_s accounts for vibrational energy. Neglecting viscosity and the magnetic field, the evolution of each species is described by following coupled continuity equations: [14]

$$\partial_t n_s + \nabla \cdot (n_s \mathbf{v}_s) = N_s \tag{2}$$

$$\partial_t (n_s \mathbf{v}_s) + \nabla \cdot (n_s \mathbf{v}_s \mathbf{v}_s) = -\frac{\nabla P_s}{m_s} + \frac{q_s n_s}{m_s} \mathbf{E} + \mathbf{V}_s \tag{3}$$

$$\partial_t \Theta_s + \nabla \cdot (\Theta_s \mathbf{v}_s) = -P_s \nabla \cdot \mathbf{v}_s - \nabla \cdot \mathbf{h}_s + Q_s \tag{4}$$

$$\partial_t \Xi_s + \nabla \cdot (\Xi_s \mathbf{v}_s) = X_s \tag{5}$$

Here, P_s is the partial pressure of species s, $\mathbf{E}$ is the electrostatic field, and $\mathbf{h}_s$ is the heat flux. The electrostatic field is computed from

$$\nabla^2 \phi = -4\pi \sum_j q_j n_j \tag{6}$$

$$\mathbf{E} = -\nabla \phi \tag{7}$$

The pressure is found from

$$P_s = n_s T_s \tag{8}$$

where the temperature T_s is related to Θ_s by

$$T_s = \frac{2\Theta_s}{(3 + R_s) n_s} \tag{9}$$

Here, R_s is the number of rotational degrees of freedom. The terms N_s, $\mathbf{V}_s$, Q_s, and X_s result from chemical reactions and collisions. The part due to reactions is denoted by the same symbol primed, while the part due to collisions is denoted by a double-prime. For example,

$$N_s = N_s' + N_s'' \tag{10}$$

Ohmic heating, which plays a crucial role in electrical discharges, is contained in Q_s''.

B. Chemical Reactions

Given a list of chemical reactions indexed by the variable i, the reaction rates are

$$\mathcal{R}_i = \alpha_i \prod_j n_j^{r_i(j)} \tag{11}$$

where α_i is a temperature dependent rate coefficient, j varies over the reagents for reaction i, and $r_i(j)$ is the stoichiometric coefficient for reagent j of reaction i. The rates α_i are assumed to be of the form

$$\alpha_i = \alpha_{i0} T_s^{\beta_i} \exp^{-\gamma_i / T_s} \tag{12}$$

where T_s can be the temperature of any species involved in the reaction, and α_{i0}, β_i, and γ_i are constants. The source terms due to chemical reactions are

$$N_s' = \sum_i \mathcal{R}_i \left[p_i(s) - r_i(s) \right] \tag{13}$$

$$m_s\mathbf{V}'_s = \sum_i \mathcal{R}_i \left[\sum_j r_i(j) f_{isj} m_j \mathbf{v}_j - r_i(s) m_s \mathbf{v}_s\right] \tag{14}$$

$$Q'_s = \sum_i \mathcal{R}_i \left[\sum_j r_i(j) f_{isj}\left(\frac{\Theta_j}{n_j} + \hat{X}_s\frac{\Xi_j}{n_j}\right) - r_i(s)\frac{\Theta_s}{n_s} + \epsilon_i(s)\right] \tag{15}$$

$$X'_s = \left(1 - \hat{X}_s\right)\sum_i \mathcal{R}_i \left[\sum_j r_i(j) f_{isj}\frac{\Xi_j}{n_j} - r_i(s)\frac{\Xi_s}{n_s}\right] \tag{16}$$

where $p_i(s)$ is the stoichiometric coefficient for product s of reaction i, $\epsilon_i(s)$ is the partial heat of reaction for species s, and f_{isj} is the fraction of the energy lost by reagent j that goes into species s. The operator $\hat{X}_s$ simply evaluates to zero for species with vibrational degrees of freedom, and unity for species without vibrational degrees of freedom. Note that conservation of energy and momentum requires that $\sum_s f_{isj} = 1$.

As an example, suppose reaction $i = 1$ corresponds to three body attachment, which has the equation $e^- + O_2 + O_2 \rightarrow O_2^- + O_2$. Let the e^- index be $j = 1$, the O_2 index be $j = 2$, and the O_2^- index be $j = 3$. Then $r_1(1) = 1$ and $r_1(2) = 2$, so that $\mathcal{R}_1 = \alpha_1 n_1 n_2^2$. The attachment energy is accounted for by $\epsilon_1(3) = 0.44$ eV. The energy and momentum lost by e^- and O_2 is gained by O_2^-, so that $f_{131} = f_{132} = 1$.

C. Collisions

The part of the source term for the momentum equation due to collisions is

$$\mathbf{V}''_s = \sum_j n_j n_s \sigma_{sj}\left(\frac{T_s}{m_s} + \frac{T_j}{m_j}\right)^{1/2}(\mathbf{v}_j - \mathbf{v}_s) \tag{17}$$

where σ_{sj} is the cross section for collisions of species s with species j. For electron-neutral collisions, the cross section is taken to be constant at 5×10^{-15} cm^2. Momentum is conserved if the neutral-electron cross section is smaller by the mass ratio. For Coulomb collisions,

$$\sigma_{sj} = \frac{4\sqrt{2\pi}q_s^2 q_j^2 \ln\Lambda}{3m_s}\left(\frac{1}{m_s} + \frac{1}{m_j}\right)\left(\frac{T_s}{m_s} + \frac{T_j}{m_j}\right)^{-2} \tag{18}$$

where $\ln\Lambda$ is the Coulomb logarithm. The heating term due to collisions is

$$Q''_s = \sum_j \nu_{sj} n_j n_s (T_j - T_s) + \sum_k m_s \mathbf{V}''_s \cdot (\mathbf{v}_k - \mathbf{v}_s) - \sum_l X''_l \tag{19}$$

where ν_{sj} is the coefficient of thermal equilibration, the second term accounts for heating due to friction (including ohmic heating), and the index l varies over species that exchange vibrational energy with the thermal energy of species s. The thermal equilibration coefficient is related to the collision cross section by

$$\nu_{sj} = \frac{3\sigma_{sj} m_s}{m_s + m_j} \left(\frac{T_s}{m_s} + \frac{T_j}{m_j} \right)^{1/2} \tag{20}$$

The vibrational source term is

$$X_s'' = n_s \epsilon_v \left(1 - e^{-\epsilon_v/\Psi_s}\right) \sum_\nu \chi_\nu n_j \nu \left[1 - \exp\left(\frac{\epsilon_v \nu}{T_j} - \frac{\epsilon_v \nu}{\Psi_s} \right)\right] \tag{21}$$

where Ψ_s is the vibrational temperature, ν is the vibrational level, ϵ_v is the energy between adjacent vibrational levels, j indexes the species that excites the vibration, and χ_ν is a two-body rate coefficient which depends on T_j through

$$\chi_\nu = \hat{P} \left(\sum_{i=1}^{4} c_{i\nu} T_j^i \right) \exp\left(-c_{5\nu} T_j\right) \tag{22}$$

This form was found to give satisfactory fits to the tabulated data of Ref. [15]. The operator $\hat{P}$ multiplies by zero if the operand is negative and by unity otherwise (the curve fit sometimes gives negative values for $T_j \lesssim 0.2$ eV). The vibrational temperature Ψ_s is found from

$$\Psi_s = \frac{\epsilon_v}{\ln\left(1 + \epsilon_v n_s / \Xi_s\right)} \tag{23}$$

III. IMPLICIT ELECTRON MODEL

The full electrostatic-hydrodynamic model discussed in the last section requires that the electron motion be explicitly resolved. This is computationally demanding since it requires that the timestep be small enough to resolve both the electron collision frequency and the electron plasma frequency. For example, to accurately resolve electron-neutral collisions requires a timestep of $\lesssim$ 100 femtoseconds. In this section we give a model that treats the heavy species as in the last section, but uses more efficient equations for the electrons.

The need to resolve the electron-neutral collision frequency can be removed by replacing the electron momentum equation with its equilibrium solution

$$\mathbf{v}_e = \frac{q_e n_e \mathbf{E} - \nabla P_e}{\nu_e m_e n_e} \tag{24}$$

where the subscript e refers to electrons, convection of momentum was neglected, ν_e is the aggregate collision frequency for electrons with all heavy particles, and we took

$$\mathbf{V}_e = -\nu_e n_e \mathbf{v}_e \tag{25}$$

Unfortunately, this does not necessarily improve the situation since the charge redistribution time $m_e\nu_e/4\pi n_e q_e^2$ must still be resolved. For electron densities higher than 10^{15} cm^{-3} this timescale is even shorter than the plasma period or collision time.

The need to resolve the charge redistribution time emerges when Eq. (24), the Poisson equation, and the continuity equation are combined. Let ρ be the charge density and $\mathbf{j}$ be the current density. Inserting Eq. (24) into $\mathbf{j} \approx q_e n_e \mathbf{v}_e$ gives

$$\mathbf{j} = \sigma\left(\mathbf{E} - \frac{\nabla P}{q_e n_e}\right) \tag{26}$$

where $\sigma = q_e^2 n_e/m_e\nu_e$ is the conductivity. Inserting this into the equation of charge conservation $\partial_t\rho + \nabla\cdot\mathbf{j} = 0$ and using Poisson's equation $\nabla^2\phi = -4\pi\rho$ gives

$$\left(\frac{\partial_t}{4\pi} + \sigma\right)\nabla^2\phi_1 + \nabla\phi_1\cdot\nabla\sigma = \mathbf{E}_0\cdot\nabla\sigma - \nabla\cdot(\mu_e\nabla P) \tag{27}$$

where ϕ_1 is the space charge potential, $\mathbf{E}_0$ is the known external field, and $\mu_e = q_e/m_e\nu_e$ is the electron mobility. The operator $\partial_t/4\pi + \sigma$ dictates that in regions of uniform conductivity relaxation occurs on a $1/4\pi\sigma$ timescale.

Conceptually, the simplest way to avoid resolving the charge redistribution time is to simply drop the time derivative from Eq. (27) and solve for the equilibrium ϕ_1 every timestep. This approach turns out to be ineffective, however, because the global equilibration rate is not always fast compared to other rates of interest. Another approach [16] is to solve Eq. (27) using an implicit differencing scheme (this drives the equation toward its equilibrium solution no matter how large the timestep). This results in an elliptical equation for ϕ_1 with coefficients that not only vary in time, but also have a spatial variation that is not generally separable. This is undesirable because the direct elliptical solver to be described below cannot be used on such equations. Furthermore, it is preferable from a programming point of view to use the same field solver for both the implicit electron model and the full electrostatic-hydrodynamic model.

Accordingly, the approach adopted here is to obtain ϕ from the usual Poisson equation, but obtain ρ from Eq. (27) re-written as follows:

$$(\partial_t + 4\pi\sigma)\,\rho = -\mathbf{E}\cdot\nabla\sigma + \nabla\cdot(\mu_e\nabla P) \tag{28}$$

This equation can be solved stably for timesteps $\gg 1/4\pi\sigma$ by treating the left hand side implicitly and the right hand side explicitly. This results in an equation that is very easy to solve. Further simplification can be obtained by replacing the continuity equation (2) with the quasineutrality condition

$$q_e n_e = -\sum_{s \neq e} q_s n_s \tag{29}$$

and the energy equation (4) with

$$\partial_t \Theta_e = Q_e \tag{30}$$

Note that these replacement equations apply only to the electrons. Heavy particle motion is still computed using Eqs. (2)-(5).

IV. NUMERICAL SOLUTION

A. Grid Convention

Consider a two-dimensional grid with cells indexed by i and j, and coordinate axes denoted by z and r. The interior grid cells are labeled by the set $i \in (1, 2, ..., N_z) \times j \in (1, 2, ..., N_r)$. The interior is surrounded by a single layer of ghost cells. All quantities are considered known at the cell centers. For example, $\phi_1(i, j)$ refers to the space charge potential at the center of cell (i, j).

The particular geometry of the grid does not have to be specified in formulating the problem. Instead, finite difference equations can be derived that depend on the volumes of the cells and the areas of the cell walls. These areas and volumes can be specified when the code is started, and can even be changed while the code is running. This allows a single algorithm to work on either a cartesian or cylindrical grid, and also allows the grid to change as the simulation runs. The volume of cell (i, j) is written $V(i, j)$. The area of the cell wall bounding cell (i, j) on the negative z-side is $A_z(i, j)$. The area of the cell wall bounding cell (i, j) on the negative r-side is $A_r(i, j)$. The position of the center of cell (i, j) is (z_i, r_j). It is assumed that the i-position of any cell is independent of j, and vice-versa. This is equivalent to the statement that the grid lines must be orthogonal.

B. Second Order Time Advance

The differential equations describing the evolution of all the quantities considered in the SPARC model can be put in the form

$$\partial_t \mathbf{f} = \hat{T}\mathbf{f} \tag{31}$$

where $\mathbf{f}$ is the vector of all quantities to be advanced and $\hat{T}$ is an operator that does not depend explicitly on time. Let the value of $\mathbf{f}$ at time level n be denoted $\mathbf{f}^n$. To compute $\mathbf{f}^{n+1}$ with second order accuracy, a variant of the midpoint method is used. In the usual midpoint method, a provisional value $\mathbf{f}^{n+1/2}$ is computed using

$$\mathbf{f}^{n+1/2} = \mathbf{f}^n + \frac{\Delta t}{2}\hat{T}\mathbf{f}^n \tag{32}$$

and the value at the new time level is computed using

$$\mathbf{f}^{n+1} = \mathbf{f}^n + \Delta t \hat{T}\mathbf{f}^{n+1/2} \tag{33}$$

This description is not quite adequate for SPARC because of the subtleties involved in evaluating certain equations. However, the midpoint method can be easily generalized as follows. Suppose we have an operator $\hat{F}(\Delta t, \mathbf{g})$ that advances $\mathbf{f}^n$ by a time interval Δt using $\mathbf{g}$ as the vector of quantities to be used in evaluating the right hand side of Eq. (31). Suppose further that if $\mathbf{g} = \mathbf{f}^n$, the advance is first order accurate:

$$\mathbf{f}^{n+1} = \hat{F}(\Delta t, \mathbf{f}^n)\mathbf{f}^n + O(\Delta t) \tag{34}$$

Then, second order accuracy is achieved by using

$$\mathbf{f}^{n+1/2} = \hat{F}\left(\frac{\Delta t}{2}, \mathbf{f}^n\right)\mathbf{f}^n + O(\Delta t) \tag{35}$$

$$\mathbf{f}^{n+1} = \hat{F}(\Delta t, \mathbf{f}^{n+1/2})\mathbf{f}^n + O(\Delta t^2) \tag{36}$$

It remains only to identify the components of $\hat{F}$ with the first order algorithms that are used to advance the quantities of interest.

C. Finite Difference Form of Divergence and Laplacian

The finite difference form of the divergence of a discrete vector field $\mathbf{E}(i, j)$ defined on any grid where the geometry is specified as above is

$$\nabla \cdot \mathbf{E} = -D_1 E_z(i - 1/2, j) + D_2 E_z(i + 1/2, j) - D_3 E_r(i, j - 1/2) + D_4 E_r(i, j + 1/2) \tag{37}$$

where the subscripts on E select a vector component, and

$$D_1(i,j) = A_z(i,j)/V(i,j) \tag{38}$$

$$D_2(i,j) = A_z(i+1,j)/V(i,j) \tag{39}$$

$$D_3(i,j) = A_r(i,j)/V(i,j) \tag{40}$$

$$D_4(i,j) = A_r(i,j+1)/V(i,j) \tag{41}$$

Note that the arguments of $D_1 \ldots D_4$ were suppressed in Eq. (37). Also, fractional indices indicate that an average is to be taken over the values corresponding to the two nearest integral indices. For example,

$$E_z(i-1/2,j) = E_z(i-1,j)/2 + E_z(i,j)/2 \tag{42}$$

The form of the Laplacian consistent with this definition of the divergence is found by substituting

$$E_z(i-1/2,j) = (\phi(i-1,j) - \phi(i,j))/\Delta_{i-1/2} \tag{43}$$

$$E_z(i+1/2,j) = (\phi(i,j) - \phi(i+1,j))/\Delta_{i+1/2} \tag{44}$$

$$E_r(i,j-1/2) = (\phi(i,j-1) - \phi(i,j))/\Delta_{j-1/2} \tag{45}$$

$$E_r(i,j+1/2) = (\phi(i,j) - \phi(i,j+1))/\Delta_{j+1/2} \tag{46}$$

into the formula for the divergence. Here we have defined

$$\Delta_{i+1/2} = z_{i+1} - z_i \tag{47}$$

$$\Delta_{j+1/2} = r_{j+1} - r_j \tag{48}$$

This gives for the Laplacian

$$\nabla^2\phi = \frac{D_1\phi(i-1,j)}{\Delta_{i-1/2}} + \frac{D_2\phi(i+1,j)}{\Delta_{i+1/2}} + \frac{D_3\phi(i,j-1)}{\Delta_{j-1/2}} + \frac{D_4\phi(i,j+1)}{\Delta_{j+1/2}} + D_5\phi(i,j) \tag{49}$$

where

$$D_5 = -\left(\frac{D_1}{\Delta_{i-1/2}} + \frac{D_2}{\Delta_{i+1/2}} + \frac{D_3}{\Delta_{j-1/2}} + \frac{D_4}{\Delta_{j+1/2}}\right) \tag{50}$$

D. Poisson Solver

The Poisson solver used in SPARC takes advantage of the fact that for the problem of interest, $N_z \gg N_r$, where we now associate z with the axial direction and r with the radial. Even with an adaptive grid, the number of axial cells is still much greater than the number of radial cells because the cell size has to be changed gradually to maintain accuracy. SPARC takes advantage of $N_z \gg N_r$ by solving the Poisson equation using a technique that requires $O(N_z N_r^2)$ operations. Since N_r is not too large (≈ 100), the technique works well. In fact, it turns out that the Poisson solver does not dominate the computation time in most cases. Unlike iterative methods, the approach developed here gives the solution to within machine precision in a fixed number of operations. It also parallelizes well via domain decomposition in the axial direction.

The finite difference form of the Poisson equation can be put in the form of a matrix equation if $\phi(i,j)$ and $\rho(i,j)$ are regarded as matrices where i is the axial (column) index and j is the radial (row) index. The matrix form of the Poisson equation is

$$R\phi + \left(Z\phi^T\right)^T = -4\pi\rho \tag{51}$$

where R is the radial part of the Laplacian operator written in matrix form and Z is the axial part. The superscript T indicates that the transpose is to be taken. The matrices R and Z are

$$Z_{im} = \begin{cases} D_1(i)/\Delta_{i-1/2} & m = i-1 \\ -D_1(i)/\Delta_{i-1/2} - D_2(i)/\Delta_{i+1/2} & m = i \\ D_2(i)/\Delta_{i+1/2} & m = i+1 \\ 0 & \text{otherwise} \end{cases} \tag{52}$$

$$R_{jm} = \begin{cases} D_3(j)/\Delta_{j-1/2} & m = j-1 \\ -D_3(j)/\Delta_{j-1/2} - D_4(j)/\Delta_{j+1/2} & m = j \\ D_4(j)/\Delta_{j+1/2} & m = j+1 \\ 0 & \text{otherwise} \end{cases} \tag{53}$$

Here the requirement emerges that D_1 and D_2 be independent of j, and D_3 and D_4 be independent of i. This requirement will always be met provided the grid lines are orthogonal. We now arrange the eigenvectors of R in columns to form a matrix denoted by H^{-1}. This matrix has the property that

$$HRH^{-1} = \Lambda \tag{54}$$

where Λ is diagonal. Multiplying the Poisson equation by H on the left hand side causes the problem to decouple into N_r independent one dimensional problems:

$$\frac{D_1}{\Delta_{i-1/2}}\hat{\phi}(i-1,j) - \left(\frac{D_1}{\Delta_{i-1/2}} + \frac{D_2}{\Delta_{i+1/2}} - \Lambda_j\right)\hat{\phi}(i,j) + \frac{D_2}{\Delta_{i+1/2}}\hat{\phi}(i+1,j) = -4\pi\hat{\rho}(i,j) \quad (55)$$

where $\hat{\phi} = H\phi$ and $\hat{\rho} = H\rho$. This equation can be solved by the usual tridiagonal algorithm. This leads to the following procedure for obtaining ϕ given ρ:

1. Diagonalize R and store the eigenvalues Λ_j and the matrices H and H^{-1}. We do this using the QR algorithm and inverse iteration. Since the radial grid spacings do not evolve, R stays constant throughout the simulation and this can be done once at the beginning.
2. Form the transformed charge density $\hat{\rho} = H\rho$. This takes $O(N_z N_r^2)$ operations.
3. Solve the tridiagonal system (55) for $\hat{\phi}$. This takes $O(N_z N_r)$ operations.
4. Form the solution in real space, $\phi = H^{-1}\hat{\phi}$. This takes $O(N_z N_r^2)$ operations.

Note that if the bounded discrete space considered here is replaced by an unbounded continuous space, H becomes the Hankel transform of zero order.

E. Fluid Advance and Chemistry

The fluid equations (2)-(5) are advanced using the well known method of flux corrected transport (FCT). The particular variant of FCT used is essentially a C++ rewrite of the LCPFCT (NRL Laboratory for Computational Physics and Fluid Dynamics FCT) routine [17]. The routine is extended to two dimensions using the operator splitting approach described in Ref. [17].

The source terms for the fluid equations include terms following directly from the Boltzmann equation, such as the heat flux term, as well as terms that are put in "by hand" to account for chemical reactions. These terms can all be found by straightforward differencing. Of course, the differencing has to account for variations in the grid geometry in the manner described above.

F. Sliding Rezone

A streamer generally consists of an elongated region called the "body" in which the axial derivatives ∂_z are small, and a much shorter region at the end of the body (the "tip") where ∂_z is large. The sliding rezone technique minimizes the number of grid cells needed to model the streamer by using large cells in the body and small cells in the tip. The technique works by keeping the total number of axial grid cells, N_z, constant, while varying the spacing between the grid cells as the simulation runs.

The function giving the length of the i^{th} grid cell is

$$\Delta z_i = \Delta z \begin{cases} 1 + Af\left(\frac{i-1}{N-1}\right) & 0 < i \leq N & \text{“Region1”} \\ 1 + Bf\left(\frac{i-N-1}{N-1}\right) & N < i \leq 2N & \text{“Region2”} \\ 1 & 2N < i \leq 3N & \text{“Region3”} \\ 1 + Cf\left(\frac{i-3N-1}{N-1}\right) & 3N < i \leq 4N & \text{“Region4”} \end{cases}$$

where Δz is the minimum cell length, $N = N_z/4$ is the number of cells in each region, and the function f is a smooth polynomial that ramps from zero to one and back to zero according to

$$f(\tau) = \begin{cases} 10(2\tau)^3 - 15(2\tau)^4 + 6(2\tau)^5 & 0 \leq \tau \leq 1/2 \\ 1 - 10(2\tau-1)^3 + 15(2\tau-1)^4 - 6(2\tau-1)^5 & 1/2 < \tau \leq 1 \\ 0 & \text{otherwise} \end{cases}$$

The grid is modified as the simulation runs by varying the parameters A, B, and C. Thus, the resolution in regions 1, 2, and 4 can be changed, but region 3 is always kept at the highest resolution.

Region 1 is used to contain the initial streamer. It does not evolve during the course of the simulation. It contains a high resolution region at both ends. The high resolution sub-region near the electrode ($i = 1$) is not currently needed, but can be used in the future to support a sheath model. The sub-region near $i = N$ is kept at high resolution due to the fact the streamer tip leaves perturbations at its initial location long after it has propagated away. The constant characterizing region 1, A, is specified at the beginning of the simulation and does not have to be changed thereafter. In particular,

$$A = \frac{1}{S}\left(\frac{L_1}{\Delta z} - N\right) \tag{56}$$

where

$$S = \sum_{i=1}^{N} f\left(\frac{i-1}{N-1}\right) \tag{57}$$

and L_1 is the desired length of region 1.

Region 2 is used to contain the streamer body. Early in the simulation, the tip propagates through this region, so the highest resolution is needed. Therefore the parameter B is initially set to zero. Once the tip reaches the center of region 3, however, B is increased such that the tip stays centered in region 3. In particular, when the code detects that the peak of the axial electric field has moved more than one grid cell beyond the center of region 3, a new value of B is calculated using

$$B = \frac{1}{S}\left(\frac{z_0}{\Delta z} - \frac{5N}{2} + 1 - AS\right) \tag{58}$$

where

$$z_0 = \Delta z\left(\frac{5N}{2} + AS + B'S\right) \tag{59}$$

and B' is the old value of B. The new value of B is chosen to shift the cells in region 3 by an amount Δz. The parameter z_0 is the location of the center of region 3 before the shift.

Region 3 stays at the highest resolution throughout the simulation, and is used to contain the streamer tip. This is the high resolution region that "slides" forward with the tip as the parameter B is increased.

Region 4 is used to model the space between the streamer tip and the "ground" electrode. At the start of the simulation this region is at its largest, and the parameter C is chosen to make the end of the simulation box coincide with the desired position of the ground. In particular,

$$C = \frac{1}{S}\left(\frac{L_{\text{tot}}}{\Delta z} - 4N - AS - BS\right) \tag{60}$$

where L_{tot} is the total length of the simulation box. This has to be re-evaluated every time B changes. That is, in order to keep L_{tot} constant, C has to be reduced every time B is increased

G. Boundary Conditions

For the Poisson equation and the hydrodynamic equations boundary conditions are needed. For the hydrodynamic quantities the normal derivative is taken to vanish at all boundaries. For the virtual boundary at $r = 0$, the normal derivative vanishes for scalars and the quantity itself vanishes for vectors. These boundary conditions allow fluid to flow freely into or out out of any boundary. In reality, there would be a sheath near the electrode which we neglect.

In the case of the Poisson solver, the boundary conditions are chosen so that in the absence of space charge, the field is consistent with that produced by a spherical electrode. However, this can only be done approximately because of the shape of the grid lines. In particular, the potential in any cell is

$$\phi(i,j) = \phi_0(i,j) + \phi_1(i,j) \tag{61}$$

$$\phi_0(i,j) = \frac{R_e \phi_{00}}{\sqrt{r_j^2 + (R_e + z_i)^2}} \tag{62}$$

where ϕ_1 is the space charge potential, ϕ_0 is the potential in the absence of space charge, R_e is the radius of the electrode, and ϕ_{00} is the potential at the surface of the electrode. The expression for ϕ_0 is taken to be valid both in the interior and on the boundaries, while ϕ_1 is assumed to vanish at the boundaries. For the virtual boundary at $r = 0$, the normal derivative vanishes. This formulation is valid if $r_j \ll R_e$ for all j since then the surface of the electrode nearly coincides with the planar boundary of the grid.

A real air discharge can often be considered radially unbounded. It is therefore desirable to move the radial simulation boundary as far from the axis as possible. In order to do this while keeping the number of radial grid cells small, the cell spacings are increased with increasing r. In particular, the radial cell size Δr_j is taken to vary as

$$\Delta r_j = \begin{cases} \Delta r_0 & 0 \le j \le N_u \\ \Delta r_0 (1 + \delta_r)^{j - N_u} & N_u < j \le N_r + 1 \end{cases} \tag{63}$$

where Δr_0 determines the highest resolution, N_u is the number of cells in the region of uniform resolution, and δ_r is a number which determines how fast the cells grow for $j > N_u$. Note that the ghost cells $j = 0$ and $j = N_r + 1$ are included in the definition. For the examples in this report we use $\delta_r = 0.1$.

H. Parallelization

Parallelization of SPARC is accomplished via two-dimensional domain decomposition. That is, the two-dimensional grid is divided into $N_p = N_{pz} \times N_{pr}$ subgrids. The total number of subgrids N_p is usually set equal the number of available processors so that each processor calculates all the quantities on a single subgrid. On processors that support simultaneous multi-threading (SMT, sometimes called "hyperthreading") it is advantageous to to assign multiple subgrids to each processor.

Since the equations on each subgrid are not independent of one another, information has to be exchanged between processors. The turboWAVE framework, on which SPARC is built, supports two communications methods. For shared memory systems, POSIX threads ("ptrheads") are used. For distributed memory systems, the Message Passing Interface (MPI) is used.

The SPARC module most difficult to parallelize via domain decomposition is the Poisson solver. This is because the potential in any grid cell depends on the charge density in every other grid cell. In order to divide the domain in the radial direction, the well known transpose technique is used. To divide the domain in the axial direction, we use the turboWAVE parallel tridiagonal solver described in Ref. [18].

The hydrodynamics module parallelizes via domain decomposition in a straightforward way. This is because each grid cell is updated using only information from itself and its nearest neighbors (in one evaluation the next-nearest neighbor is also needed). Hence, the cells in the interior of a subgrid can be advanced one time level independently of the other subgrids. The ghost cells are then obtained by receiving the corresponding interior cell from the adjacent subgrid. This exchange of information is carried out in a separate sweep for each direction of the domain decomposition.

Finally, the chemistry module parallelizes trivially. That is, the reaction rate in a cell depends only on quantities in the same cell. Hence, each subgrid can update itself independently of the others.

V. BENCHMARKING

Due to the complexity of SPARC, it is important to benchmark as many of the individual computational elements of the code as possible. In the following sections we show that the individual components give the expected results in cases where either an analytical result is known, a general trend is expected, or a comparison with another code can be made.

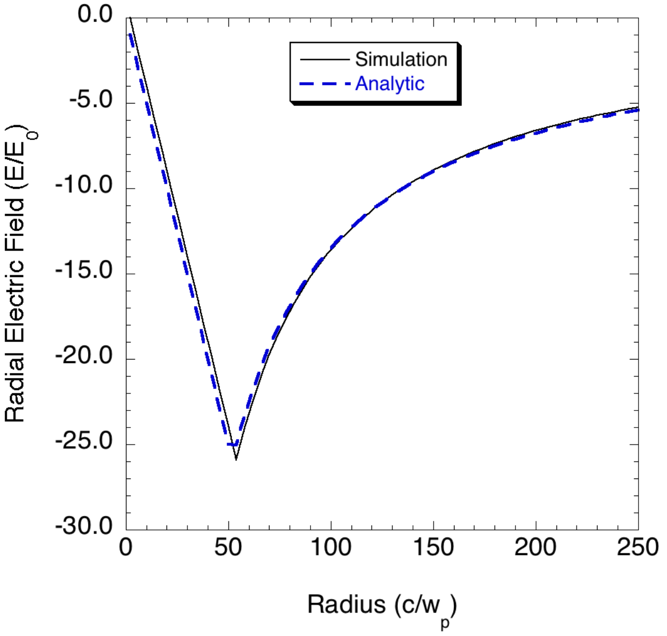

FIG. 1: Comparison of simulated and theoretical radial electric fields due to a long cylinder.

A. Poisson Solver

The simplest test to perform is to verify that the Poisson solver gives the correct electrostatic field in some analytically tractable limiting cases. As an example, Fig. 1 shows the simulated and theoretical radial electric field due to a uniformly charged cylinder with a radius small compared to its length. The agreement is satisfactory. We have also compared the fields calculated by SPARC with those calculated using the Fourier Analysis and Cyclic Reduction (FACR) technique and found the two results to be nearly indistinguishable. We further verified that the results obtained on a non-uniform grid are consistent with those obtained on a uniform grid.

B. Chemistry

Chemical reactions in SPARC are defined in the input file and not by the code itself. Specifically, when the code starts it reads the input file and creates an instance of the same C++ object for each reaction defined therein. Chemical species are handled the same way.

Hence, to benchmark the objects pertaining to chemistry it is sufficient to check just a few reactions. For example, we checked that the ionization rate was computed correctly for various values of the field and gas density. A more interesting test was to verify that the electron cooling rate was consistent with that predicted by CHMAIR II. In the initial testing it was assumed that nitrogen vibrations were the main sink of electron energy. This turned out to be a poor assumption when the electron temperature is high, as illustrated in Fig. 2(a). By accounting for the energy lost to electronic excitations into triplet states, the much improved agreement shown in Fig. 2(b) was obtained. Most of the remaining disagreement appears to be due to the use of different coefficients for the vibrational excitations. SPARC currently uses the tables from Ref. [15], while CHMAIR II uses those from Ref. [19].

C. Electrodynamics

The primary electrodynamic effect relevant to streamer and leader propagation is the development of a charged tip which leads to field enhancement. To observe this field enhancement in SPARC, we initialize a plasma filament into the simulation box with all chemical reactions turned off, and apply a constant external electric field. The density in the plasma filament is of the form $n_e(z,r) = n_s f(z) g(r)$ where

$$f(z) = \begin{cases} 1 & 0 \le z \le L_s \\ 1 - (10\zeta^3 - 15\zeta^4 + 6\zeta^5) & L_s < z \le L_t \\ 0 & \text{otherwise} \end{cases}$$

$$\zeta = \frac{z - L_s}{L_t - L_s}$$

$$g(r) = \begin{cases} 1 & 0 \le r \le R_s \\ 1 - (10\zeta_r^3 - 15\zeta_r^4 + 6\zeta_r^5) & R_s < r \le R_t \\ 0 & \text{otherwise} \end{cases}$$

$$\zeta_r = \frac{r - R_s}{R_t - R_s}$$

This represents a uniform cylinder of length L_s and radius R_s, together with axial and radial transition regions of dimension $L_t - L_s$ and $R_t - R_s$, respectively. We vary L_s and n_s, while holding fixed $L_t - L_s = 25\ \mu\text{m}$, $R_t - R_s = 25\ \mu\text{m}$, and $R_s = 25\ \mu\text{m}$. The filament is initialized in contact with the electrode where it is assumed all normal derivatives vanish (we ignore

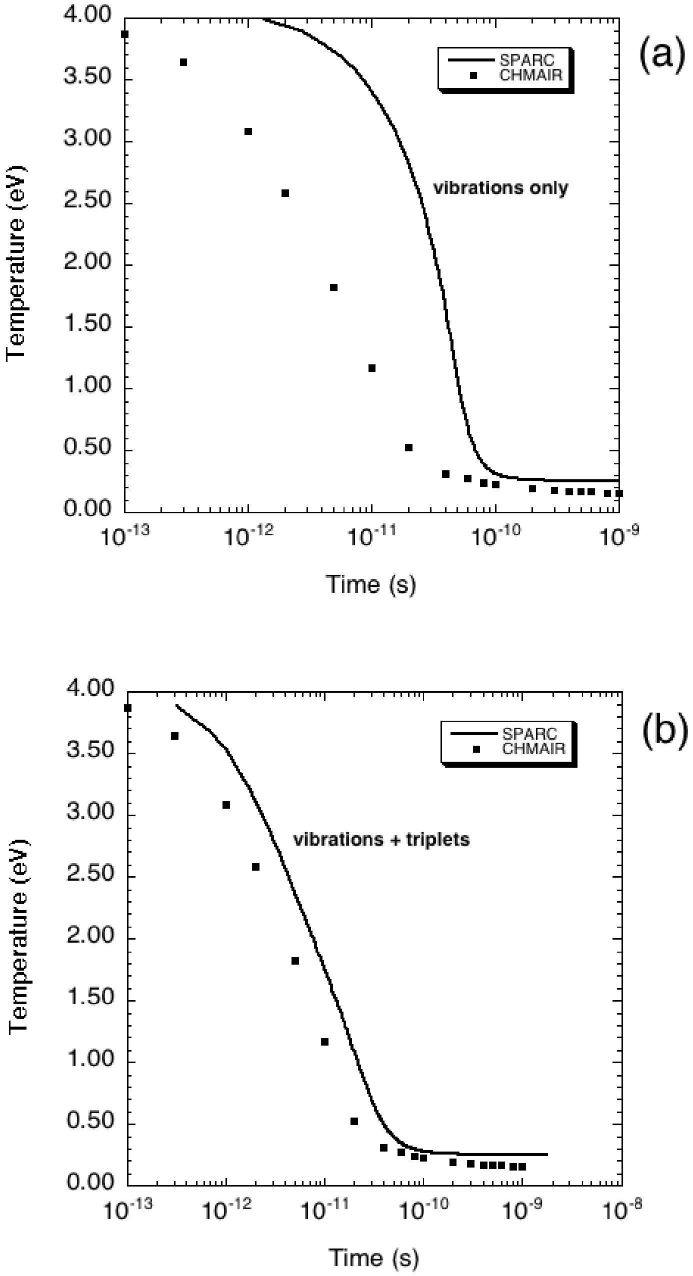

FIG. 2: Comparison of electron cooling rate as computed by SPARC and CHMAIR II: (a) before including electronic excitations (b) with electronic excitations.

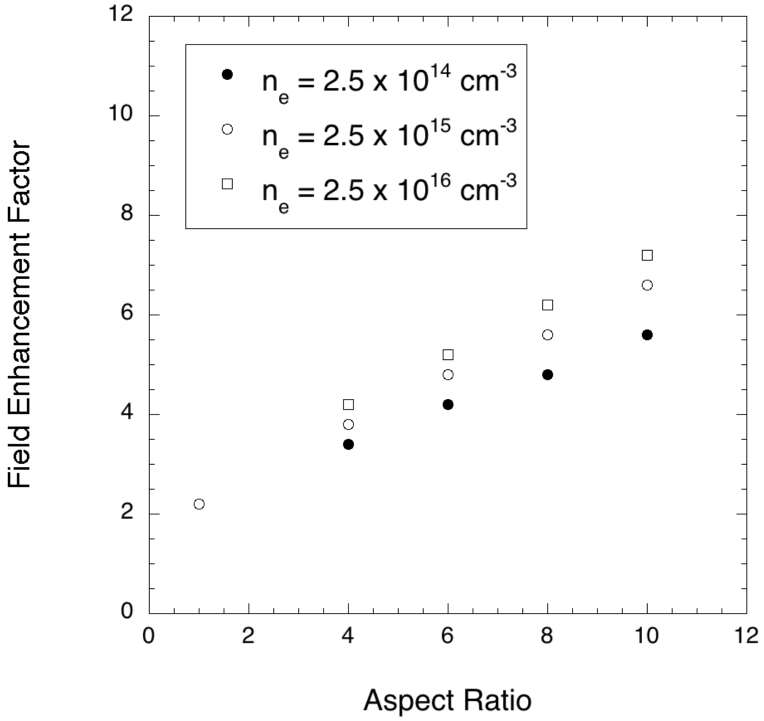

FIG. 3: Field enhancement factor for various aspect ratios and plasma densities.

the sheath). The aspect ratio is defined as $a = L_s/R_s$. Figure 3 plots the field enhancement factor as a function of the aspect ratio for three plasma densities. As expected, the field enhancement factor is of the order of the aspect ratio. It increases with both aspect ratio and plasma density.

Another electrodynamics benchmark that was performed was to measure the field relaxation time in the body of the plasma filament. We verified that the field varies as $E = E_0 e^{-t/t_0}$, where E_0 is the initial applied field, and $t_0 \approx RC$ is a constant that depends on the plasma density and geometry. Here, RC is the product of the resistance and capacitance of the plasma filament. The RC constant for a large aspect ratio uniformly conducting cylinder is

$$RC \approx 2t_r \frac{a^2}{\ln a} \tag{64}$$

where $t_r = 1/4\pi\sigma$ is the charge redistribution time and a is the aspect ratio. Figure 4 shows that the simulated field decays at this rate to within a factor of two. The factor of two discrepancy is not surprising given the approximate nature of the theoretical expression. Figure 5 shows a similar comparison holding the aspect ratio fixed at 10 and varying the electron density (and hence the conductivity).

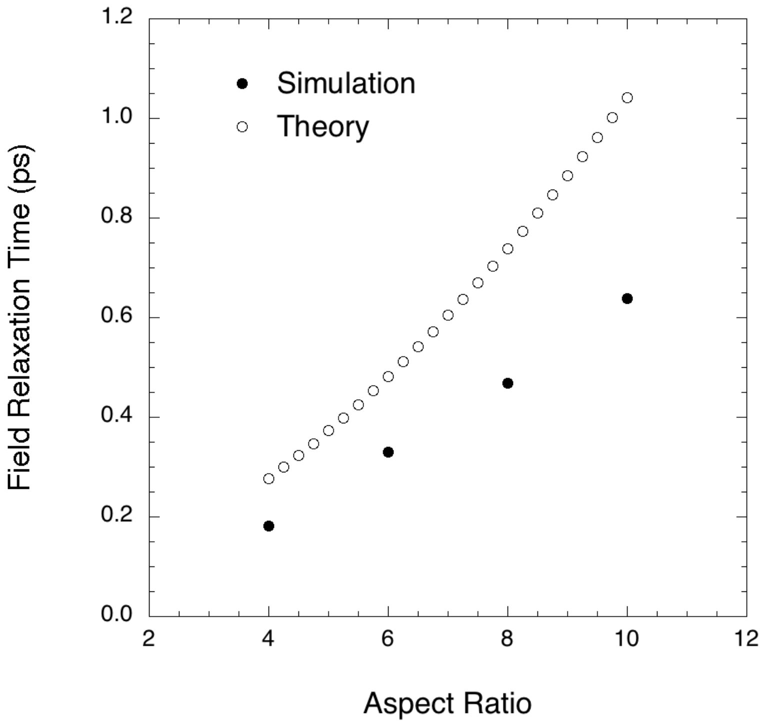

FIG. 4: Field relaxation time vs. aspect ratio for an electron density of 2.5×10^{16} cm^{-3}. The corresponding charge redistribution time is 0.012 ps.

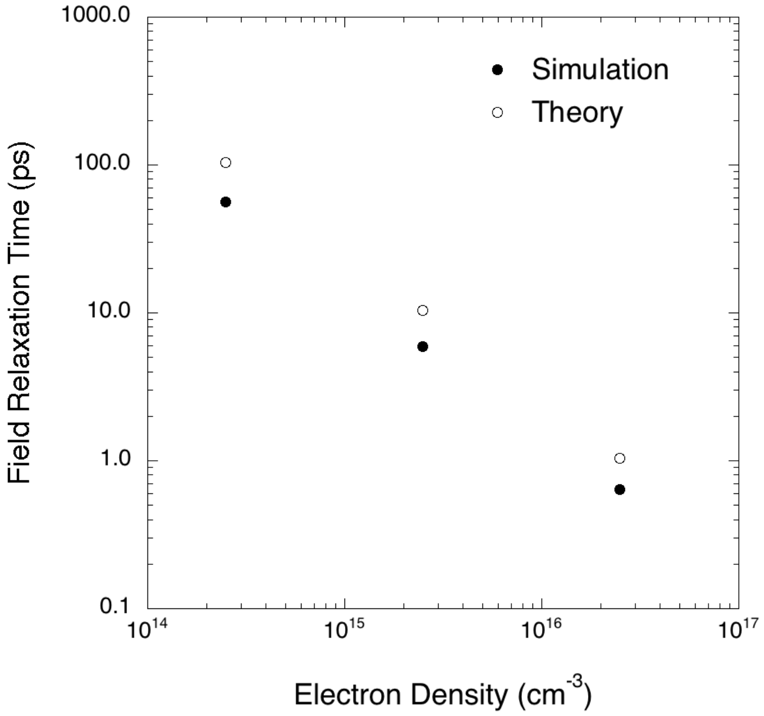

FIG. 5: Field relaxation time vs. electron density for an aspect ratio of 10.

D. Adaptive Grid

The sliding rezone algorithm was tested by performing a simulation that can be done both on a uniform grid and on an adaptive grid and comparing the two results. This simulation models streamer propagation under the assumption that the ionization rate depends on E/n_g where E is the electric field and n_g is the gas density (this assumption is removed later). Also, a generic molecule M_2 is used to represent either oxygen or nitrogen. The parameters of the simulation are given in Table I. For this simulation and for the rest of this report, the functional form of the initial plasma density is

$$n_e(z,r) = n_s f(z) e^{-r^2/r_0^2} + n_h e^{-r^2/r_h^2} + n_b \tag{65}$$

where

$$f(z) = \begin{cases} 1 & 0 \le z \le L_s \\ 1 - \frac{n_s - n_f}{n_s}\left(10\zeta^3 - 15\zeta^4 + 6\zeta^5\right) & L_s < z \le L_t \\ n_f/n_s & \text{otherwise} \end{cases}$$

$$\zeta = \frac{z - L_s}{L_t - L_s}$$

These parameters are interpreted as follows: n_s is the plasma density in the streamer, n_f is the density of the pre-ionization ahead of the streamer, n_b is a uniform background, L_s is the length of the streamer body, L_t is the length of the streamer body plus tip, and r_0 is the streamer radius. The second term can be used to include a halo due to the radiation surrounding the streamer, although in this example $n_h = 0$. The result of the benchmark is shown in Fig. 6. The results from the adaptive grid are nearly identical to those from the uniform grid. However, the uniform grid used 10^6 grid cells to model a 5 cm long region, while the adaptive grid used only 10^5 grid cells to model a 6.5 cm long region.

E. Implicit Model vs. Explicit Model

The final benchmark considered in this report is a comparison of the implicit electron model with the full electrostatic-hydrodynamic model. The two models are compared in terms of their predictions regarding streamer propagation in pure nitrogen. The parameters of the two simulations are shown in Table II. The simulations include heavy particle motion. Both calculations were run on 32 processors of the IBM cluster 1600 "Kraken" at the Naval

TABLE I: Parameters for Adaptive Grid Benchmark

Parameter	Value	Comment
Electric Field	24 kV/cm	Field is uniform
Electron Mobility	1800 $\text{cm}^2/\text{V}\cdot\text{s}$	
n_s, Streamer Density	2.5×10^{16} cm^{-3}	see Eq. (65)
r_0, Streamer Radius	100 μm	$1/e$ Definition
L_s, Streamer Length	1 cm	$L_t - L_s = 100$ μm
n_f, Preionization Density	2.5×10^{15} cm^{-3}	see Eq. (65)
n_h, Halo Density	0	see Eq. (65)
n_b, Background Density	2.5×10^{9} cm^{-3}	
Ionization Rate[a]	$5 \times 10^{-8} e^{-240/E}$ cm^3/s	$e^- + M_2 \rightarrow 2e^- + M_2^+$
Attachment Rate	2.2×10^{-30} cm^6/s	$e^- + 2M_2 \rightarrow M_2 + M_2^-$
Recombination Rate	10^{-7} cm^3/s	$e^- + M_2^+ \rightarrow M_2$
N_z, Axial Cells	1000	10^4 for uniform grid
N_r, Radial Cells	100	
N_u, Uniform Cells	50	see Eq. (63)

[a] E is the electric field in kV/cm

Oceanographic Office. The explicit calculation ran for 20 hours while the implicit calculation ran for 37 minutes. A comparison of the electron temperature after 21 ns is shown in Fig. 7. The streamer tip can be identified as the hottest region on the axis. Evidently, the implicit algorithm predicts streamer velocities that are in agreement with the explicit algorithm to within about 5%. An interesting feature of the explicit result is the discontinuity that appears near the radial cell index 70 for $z > 5$ cm. A study of the time evolution of this discontinuity reveals that it is a thermal shockwave propagating radially outward. This shockwave can actually be seen in the implicit calculation also, but it is weaker and appears only at earlier times. This suggests that the implicit algorithm introduces numerical dissipation into the system.

The subtle differences between the implicitly and explicitly computed electron temperature could be due to several factors. First, explicit differencing is generally more accurate

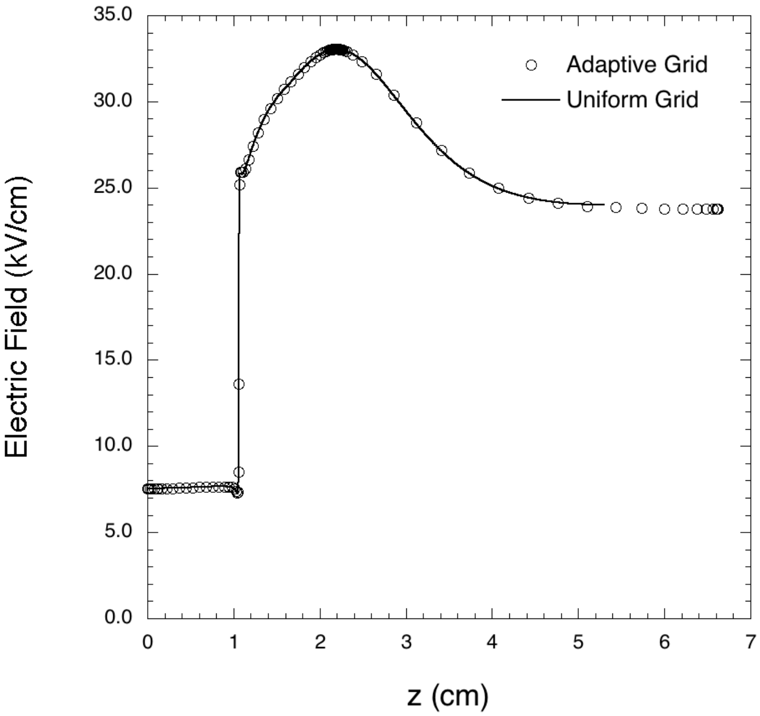

FIG. 6: Comparison of simulations using adaptive and uniform grids. The on-axis electric field at $t = 800$ ps is plotted vs. the axial coordinate, z, for both cases.

than implicit differencing. However, it was found that repeating the implicit calculation with the time-step reduced by a factor of four gave the same result. Second, the explicit calculation includes convection of electron momentum and energy density. This can occur in the tip where gradients are large, although simple estimates suggest the effect is not significant. Third, the explicit calculation allows for plasma waves since it does not assume the momentum equation is in equilibrium. Finally, the implicit calculation uses the quasineutral approximation to evaluate the electron density for use in computing chemical reaction rates. This could result in large errors in the reaction rates in a small region near the tip.

VI. SAMPLE RESULTS

In this section we give results from three SPARC simulations which use the implicit electron model. In the first example a streamer is propagated over a distance of 40 cm in the absence of attachment. In the second, a streamer to leader transition is observed with attachment included. In the third, the heavy species are allowed to move and hydrodynamic

TABLE II: Parameters for Implicit vs. Explicit Benchmark

Parameter	Value	Comment
Electrode Voltage	500 kV	constant voltage
Electrode Diameter	40 cm	spherical electrode
Electron-Neutral Cross Section	5×10^{-15} cm^2	
Ion-Neutral Cross Section	2×10^{-17} cm^2	
Electron-Ion Cross Section	see Eq. (18)	
n_s, Streamer Density	10^{16} cm^{-3}	see Eq. (65)
r_0, Streamer Radius	40 μm	$1/e$ Definition
L_s, Streamer Length	1 cm	$L_t - L_s = 100$ μm
n_f, Preionization Density	10^{15} cm^{-3}	see Eq. (65)
n_h, Halo Density	10^{9} cm^{-3}	see Eq. (65)
r_h, Halo Radius	1 cm	$1/e$ Definition
n_b, Background Density	200 cm^{-3}	
Ionization Rate[a]	$1.6 \times 10^{-8} T_e^{1/2} e^{-17.2/T_e}$ cm^3/s	$e^- + N_2 \rightarrow 2e^- + N_2^+$
Excitation Rate[b]	$5.4 \times 10^{-7} T_e^{-0.32} e^{-9.52/T_e}$ cm^3/s	$e^- + N_2 \rightarrow e^- + N_2[*]$
De-excitation Rate	3×10^{-9} cm^3/s	$N_2[*] + N_2 \rightarrow 2N_2$
Recombination Rate	$4.3 \times 10^{-8} T_e^{-0.39}$ cm^3/s	$e^- + N_2^+ \rightarrow N_2$
Vibrational Excitation	see Ref. [15]	
N_z, Axial Cells	800	
N_r, Radial Cells	150	
N_u, Uniform Cells	50	see Eq. (63)
Δt, Time Step	1.42 ps (implicit), 0.07 ps (explicit)	

[a] Temperatures are in eV

[b] $N_2[*]$ represents any triplet state

expansion is observed. In all the examples in this report, the initial temperature is 0.025 eV for heavy species, and 1 eV for electrons.

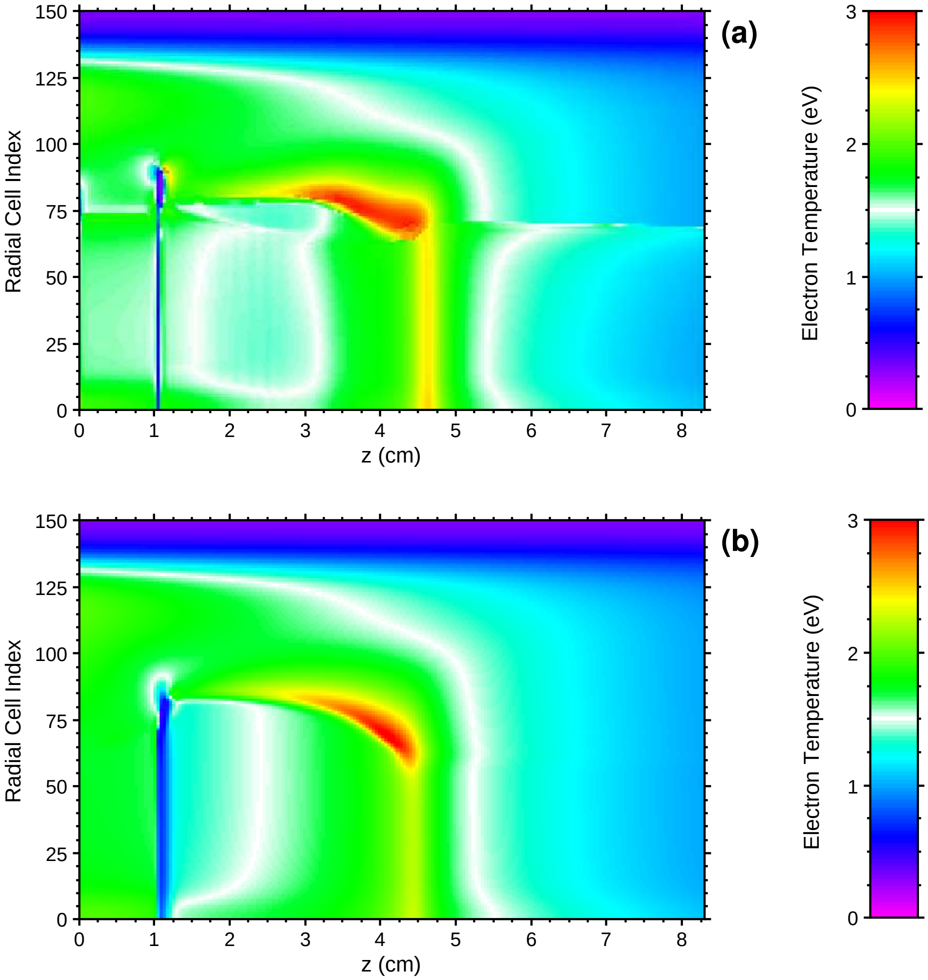

FIG. 7: Benchmark of implicit algorithm vs. explicit algorithm. Falsecolor map of the electron temperature at $t = 21$ ns for (a) explicit algorithm and (b) implicit algorithm. Note that the radial scale becomes highly nonlinear for cell indices greater than 50, as illustrated in Fig. 8.

A. Streamer Propagation

Effective streamer propagation over long distances relies on field enhancement which in turn depends on the quality of the streamer as a conductor. One criterion for a good conductor is that the electrostatic shielding distance should be much shorter than the typical dimension of the conductor. In our modeling we indeed found that streamers propagated better if they satisfied this criterion. For this reason, the streamer simulation presented here uses a radius of 0.7 mm, which is far larger than the radius of the pre-ionization associated with a femtosecond laser filament [20]. The other parameters for the simulation can be

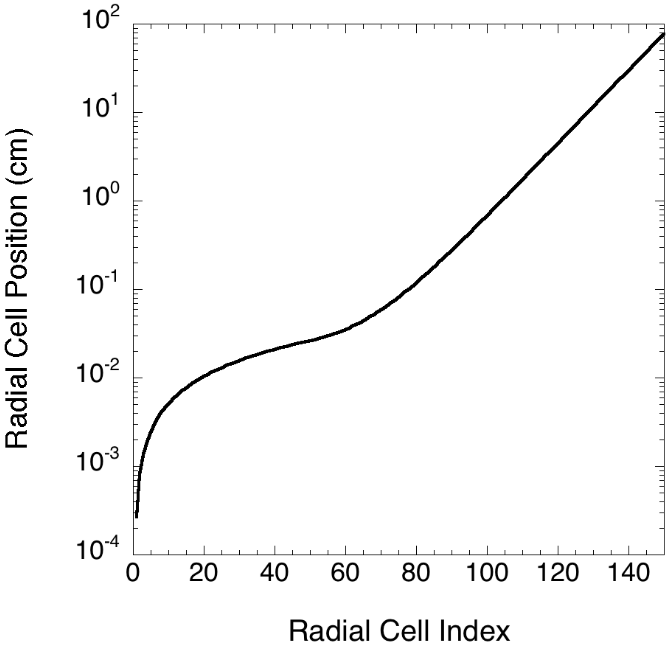

FIG. 8: Nonlinear mapping between radial cell index and position for use in interpreting Fig. 7.

found in Table III. The simulation ran for approximately 16 hours on 64 processors of the Cray XT3 "Sapphire" at the Army Engineer Research and Development Center.

The chemical reactions in Table III are taken from Refs. [15] and [19], with the following caveats. First, the excitation rate is the aggregate rate for nitrogen triplet states. The actual de-excitation mechanisms are not modeled. Instead, a fictitious collisional de-excitation mechanism which puts the excitation energy directly into the gas temperature is used. The rate associated with this interaction is chosen to give gas heating rates similar to those observed in CHMAIR simulations. Second, the recombination rates technically apply to dissociative recombination. However, since dissociated species are not included in the model, it is assumed that the dissociated species immediately re-associate, and that the ionization energy goes into heating the gas. Finally, attachment processes have not been included in this example. This can be partially justified by the fact that in an actual discharge, photo-detachment will tend to offset attachment. In fact, visible photons are easily energetic enough to detach an electron from an oxygen anion via a single photon process (the attachment energy is 0.44 eV). Since a real streamer emits visible photons, such photo-detachment is indeed expected to occur.

The on-axis electric field is plotted as a function of z for various times in Fig. 9. As

TABLE III: Parameters for Streamer Propagation Simulation

Parameter	Value	Comment
Electrode Voltage	500 kV	constant voltage
Electrode Diameter	40 cm	spherical electrode
Electron-Neutral Cross Section	5×10^{-15} cm^2	
n_s, Streamer Density	10^{14} cm^{-3}	see Eq. (65)
r_0, Streamer Radius	700 μm	$1/e$ Definition
L_s, Streamer Length	1 cm	$L_t - L_s = 100$ μm
n_f, Preionization Density	10^{12} cm^{-3}	see Eq. (65)
n_h, Halo Density	0	
n_b, Background Density	10^9 cm^{-3}	
Ionization Rate[a]	$2.2 \times 10^{-8} e^{-14.8/T_e}$ cm^3/s	$e^- + O_2 \rightarrow 2e^- + O_2^+$
Ionization Rate	$1.6 \times 10^{-8} T_e^{1/2} e^{-17.2/T_e}$ cm^3/s	$e^- + N_2 \rightarrow 2e^- + N_2^+$
Excitation Rate[b]	$5.4 \times 10^{-7} T_e^{-0.32} e^{-9.52/T_e}$ cm^3/s	$e^- + N_2 \rightarrow e^- + N_2[*]$
De-excitation Rate	3×10^{-9} cm^3/s	$N_2[*] + N_2 \rightarrow 2N_2$
Recombination Rate	$0.0019 T_e^{-0.5}$ cm^3/s	$e^- + O_2^+ \rightarrow O_2$
Recombination Rate	$4.3 \times 10^{-8} T_e^{-0.39}$ cm^3/s	$e^- + N_2^+ \rightarrow N_2$
Vibrational Excitation	see Ref. [15]	
N_z, Axial Cells	3200	
N_r, Radial Cells	150	
N_u, Uniform Cells	75	see Eq. (63)
Δt, Time Step	3.55 ps	

[a] Temperatures are in eV

[b] $N_2[*]$ represents any triplet state

expected, strong field enhancement produces a spike in the electric field indicating the tip location. At 71 ns, this field enhancement produces a field well in excess of the breakdown field. Later in time, the field enhancement is reduced as the streamer slows down. It continues to propagate even when the field is less than the breakdown field due to the fact that attachment was neglected. Fig. 10 shows the electron, vibrational, and gas temperatures after 680 ns. The electron temperature tends to follow the electric field, as is expected from theory provided the vibrational temperature remains low. As shown in the figure, the vibrational temperature, T_v, is indeed much lower than the electron temperature, T_e. Thus, the leader phase (defined by $T_v \approx T_e$) is never reached in this simulation.

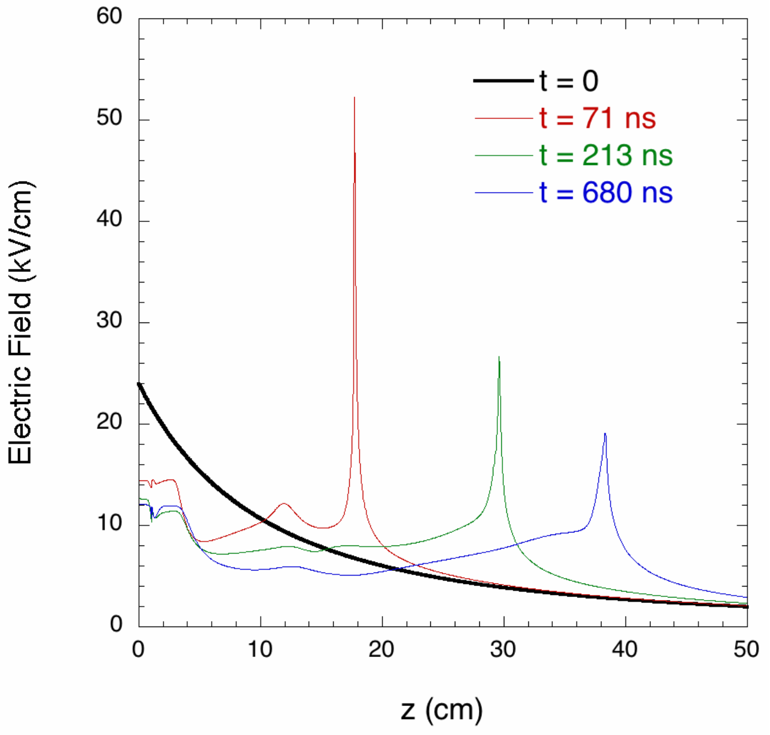

FIG. 9: Simulation of streamer propagation: on-axis E_z vs. z at various times.

B. Streamer to Leader Transition

To model the streamer to leader transition, the 40 μm radius typical of a femtosecond laser ionized filament is used as the pre-ionization radius. The voltage on the 40 cm diameter sphere starts at 500 kV and is ramped up at the rate of 570 V/ns. Other simulation parameters are given in Table IV. Note that Coulomb collisions and attachment processes are included.

The on-axis electric field is plotted as a function of z for various times in Fig. 11. The evolution of the spike in the electric field is markedly different from the case of the streamer simulation of Fig. 9. The field enhancement early in time is less effective because the diameter of the plasma is small, and therefore there is less charge available to perturb

TABLE IV: Parameters for Streamer to Leader Transition

Parameter	Value	Comment
Electrode Voltage	500 kV	570 V/ns slew rate
Electrode Diameter	40 cm	spherical electrode
Electron-Neutral Cross Section	5×10^{-15} cm^2	
Ion-Neutral Cross Section	2×10^{-17} cm^2	
Electron-Ion Cross Section	see Eq. (18)	
n_s, Streamer Density	10^{16} cm^{-3}	see Eq. (65)
r_0, Streamer Radius	40 μm	$1/e$ Definition
L_s, Streamer Length	1 cm	$L_t - L_s = 100$ μm
n_f, Preionization Density	10^{15} cm^{-3}	see Eq. (65)
n_h, Halo Density	0	
n_b, Background Density	10^9 cm^{-3}	
Ionization Rate[a]	$2.2 \times 10^{-8} e^{-14.8/T_e}$ cm^3/s	$e^- + O_2 \rightarrow 2e^- + O_2^+$
Ionization Rate	$1.6 \times 10^{-8} T_e^{1/2} e^{-17.2/T_e}$ cm^3/s	$e^- + N_2 \rightarrow 2e^- + N_2^+$
Excitation Rate[b]	$5.4 \times 10^{-7} T_e^{-0.32} e^{-9.52/T_e}$ cm^3/s	$e^- + N_2 \rightarrow e^- + N_2[*]$
De-excitation Rate	3×10^{-9} cm^3/s	$N_2[*] + N_2 \rightarrow 2N_2$
Recombination Rate	$0.0019 T_e^{-0.5}$ cm^3/s	$e^- + O_2^+ \rightarrow O_2$
Recombination Rate	$4.3 \times 10^{-8} T_e^{-0.39}$ cm^3/s	$e^- + N_2^+ \rightarrow N_2$
Vibrational Excitation	see Ref. [15]	
Attachment Rate	$3.5 \times 10^{-31} T_e^{-1} e^{-0.052/T_e}$ cm^6/s	$e^- + O_2 + O_2 \rightarrow O_2 + O_2^-$
Attachment Rate	10^{-31} cm^6/s	$e^- + O_2 + N_2 \rightarrow N_2 + O_2^-$
Detachment Rate	$4.8 \times 10^{-10} T_g^{1.5} e^{-0.43/T_g}$ cm^3/s	$N_2 + O_2^- \rightarrow O_2 + N_2 + e^-$
N_z, Axial Cells	800	
N_r, Radial Cells	150	
N_u, Uniform Cells	50	see Eq. (63)
Δt, Time Step	2.84 ps	

[a] Temperatures are in eV

[b] $N_2[*]$ represents any triplet state

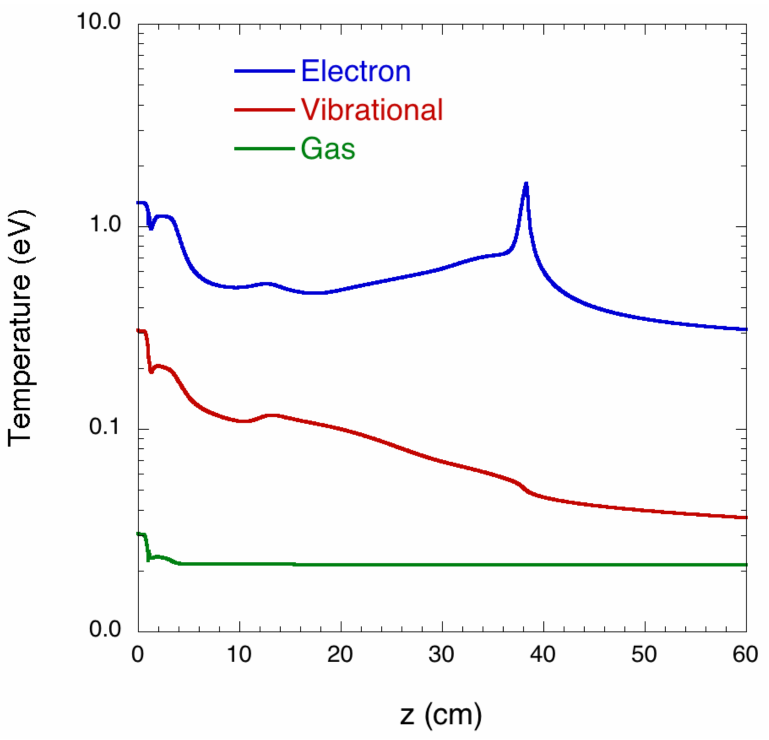

FIG. 10: Simulation of streamer propagation: on-axis temperatures vs. z after 680 nanoseconds.

the applied field. Later in time, the field enhancement increases because of the effects of attachment. Attachment reduces the electron density ahead of the streamer which leads to a more extreme gradient in charge density at the tip. This causes the electric field spike to become narrower and larger in amplitude.

The on-axis electron, vibrational, and gas temperatures after 220 ns are plotted in Fig. 12. The voltage on the sphere at this time is 625 kV. The vibrational and gas temperature are approximately 1 eV near the electrode. The vibrational temperature drops to 0.5 eV about 8 cm from the electrode. The streamer tip can be seen as the spike in electron temperature about 15 cm from the electrode. Since the vibrational temperature is high throughout a significant portion of the filament body, the transition to a leader can be considered to have occurred. Figure 13 plots the tip position as a function of time. For the first 100 ns of propagation, the tip slows down much as in the pure streamer simulation discussed above. After 100 ns, the tip propagates at a constant speed, and even appears to speed up near the end of the simulation. This behavior will be investigated further as this work continues.

Although this result is encouraging, it does not illustrate the full leader development. The missing element is the reduction of the electric field in the leader body. The electric

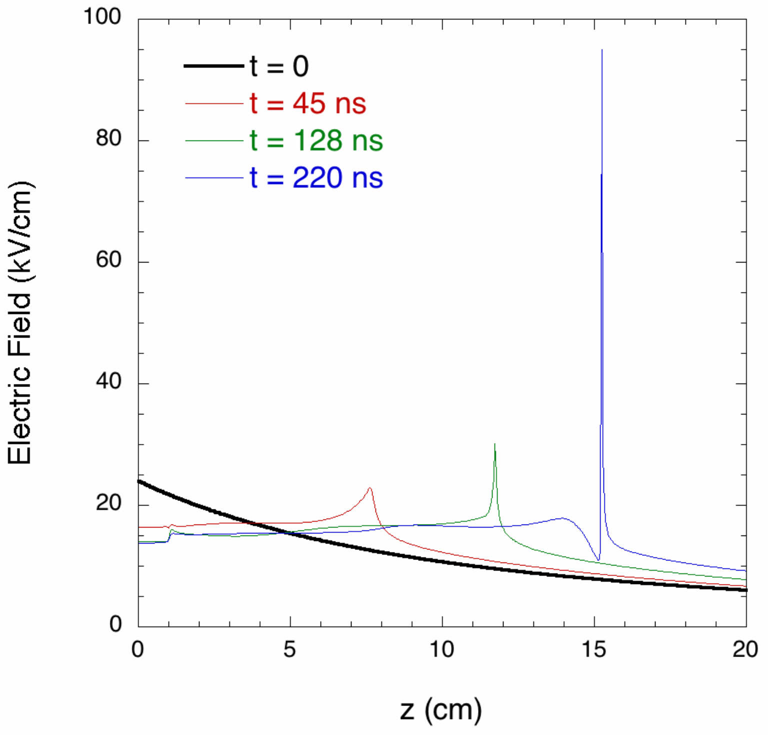

FIG. 11: Simulation of streamer to leader transition: on-axis E_z vs. z at various times. Note that the applied field increases with time.

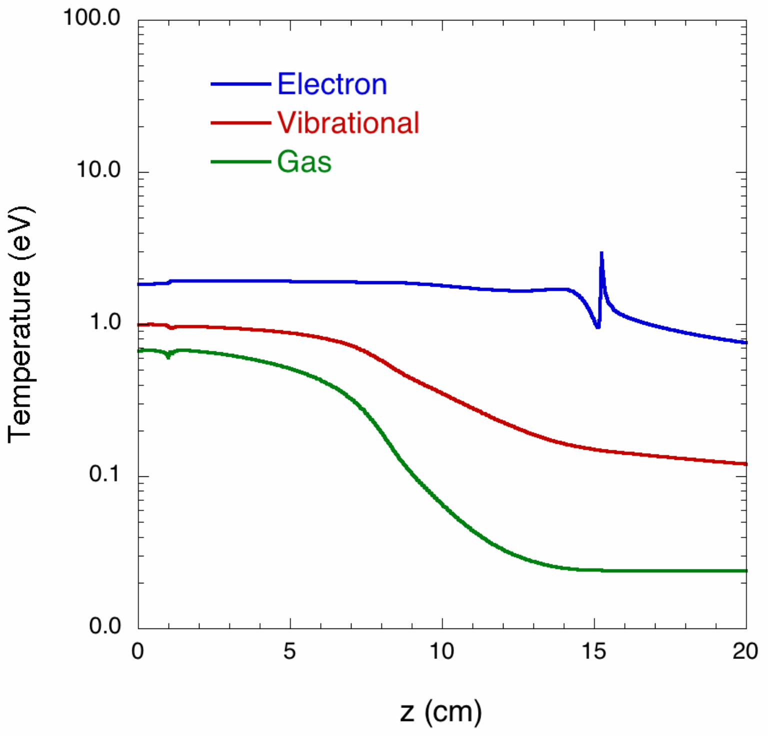

FIG. 12: Simulation of streamer to leader transition: on-axis temperatures vs. z after 220 ns.

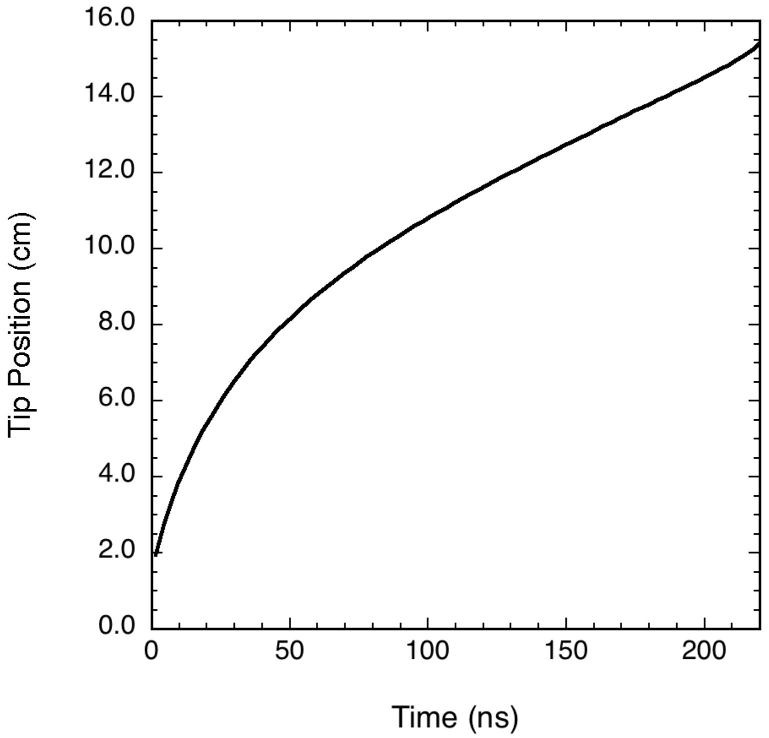

FIG. 13: Simulation of streamer to leader transition: position of streamer/leader tip vs. time.

field in the body is a constant 15 kV/cm, which is too high to allow for long propagation distances. This may be due to the small diameter of the leader body which implies a large resistance. It may be that including hydrodynamic effects, or running the simulation longer, will allow the leader body to expand radially so that the resistance is reduced.

To illustrate the hydrodynamics capability of SPARC, a short run was made with heavy particle motion enabled. The parameters are as in the leader simulation above, except that electron-ion collisions are neglected, attachment processes are neglected, and the voltage on the sphere is held fixed at +500 kV. In this simulation, heating of the gas results in hydrodynamic expansion which leads to a noticeable drop in the on-axis nitrogen density within 70 ns. This is illustrated in Fig. 14.

VII. CONCLUSIONS

A simulation code has been developed which models electrical discharges in air. The code is capable of modeling streamer propagation over long distances because of an adaptive grid, fully scalable parallelism, and an implicit model for electron motion. An example in this

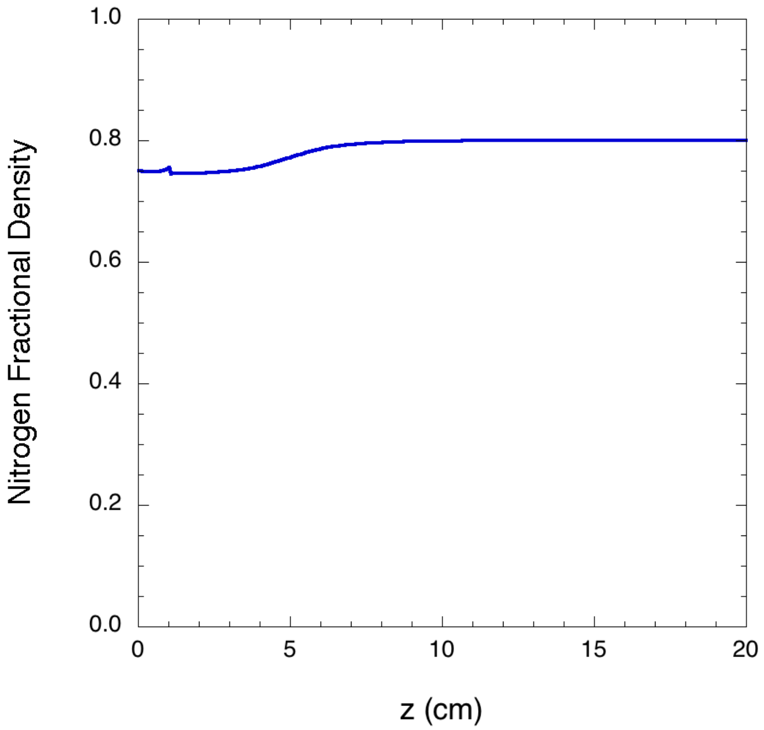

FIG. 14: Simulation with heavy particle motion: on-axis nitrogen density vs. z after 70 nanoseconds.

report shows a streamer propagating for 40 cm. The code is also capable of modeling the vibrational excitation of nitrogen and its interplay with ohmic heating of the electrons. This allows the leader phase to develop. An example in this report shows the vibrational temperature reaching about 1 eV in a several centimeter long region. However, a dramatic reduction in the on-axis electric field was not observed. Finally, a benchmark comparing the explicit and implicit models showed that the implicit model recovers the important features of the explicit model in $1/30^{\text{th}}$ of the computer time.

VIII. ACKNOWLEDGEMENTS

Useful discussions with S. Zalesak, D. Colombant, B. Hafizi, J. Peñano, J.D. Huba, R.F. Hubbard, L. Petrova, P. Lundquist, S. McCahon, and J. Hayden are gratefully acknowledged.

This work was supported by NAVSEA.

---

[1] Y.P. Raizer. *Gas Discharge Physics*. Springer, 1991.

[2] D. Comtois, C.Y. Chien, A. Desparois, F. Genin, G. Jarry, T.W. Johnston, J.-C. Kieffer, B. La Fontaine, F. Martin, R. Mawassi, H. Pepin, F.A.M. Rizk, F. Vidal, P. Couture, H.P. Mercure, C. Potvin, A. Bondiou-Clergerie, and I. Gallimberti. Triggering and guiding leader discharges using a plasma channel created by an ultrashort laser pulse. *Appl. Phys. Lett.*, 76(7):819–821, Feb 2000.

[3] B. La Fontaine, D. Comtois, C.-Y. Chien, A. Desparois, F. Genin, G. Jarry, T. Johnston, J.-C. Kieffer, F. Martin, R. Mawassi, H. Pepin, F.A.M. Rizk, F. Vidal, C. Potvin, P. Couture, and H.P. Mercure. Guiding large-scale spark discharges with ultrashort pulse laser filaments. *J. Appl. Phys.*, 88(2):610–615, July 2000.

[4] S. Tzortzakis, B. Prade, M. Franco, and A. Mysyrowicz. Femtosecond laser-guided electric discharge in air. *Phys. Rev. E*, 64:057401–1–057401–4, Oct 2001.

[5] M. Rodriguez, R. Sauerbrey, H. Willie, L. Woste, T. Fujii, T.-B. Andre, A. Mysyrowicz, L. Klingbeil, K. Rethmeier, W. Kalkner, J. Kasparian, E. Salmon, J. Yu, and J.-P. Wolf. Triggering and guiding megavolt discharges by use of laser-induced ionized filaments. *Opt. Lett.*, 27(9):772–774, May 2002.

[6] D.F. Gordon, A. Ting, R.F. Hubbard, E. Briscoe, C. Manka, S.P. Slinker, A.P Baronavski, H.D. Ladouceur, P.W. Grounds, and P.G. Girardi. Streamerless guided electric discharges triggered by femtosecond laser filaments. *Phys. Plasmas*, 10(11):4530–4538, Nov 2003.

[7] R.F. Fernsler. General model of streamer propagation. *Phys. Fluids*, 27(4):1005–1012, Apr 1984.

[8] P.A. Vitello, B.M. Penetrante, and J.N. Bardsley. Simulation of negative-streamer dynamics in nitrogen. *Phys. Rev. E*, 49(6):5574–5598, Jun 1994.

[9] R. Morrow and J.J. Lowke. Streamer propagation in air. *J. Phys. D: Appl. Phys.*, 30:614–627, 1997.

[10] N.Y. Babaeva and G.V. Naidis. Dynamics of positive and negative streamers in air in weak uniform electric fields. *IEEE Trans. on Plasma Sci.*, 25(2):375–379, Apr 1997.

[11] G.E. Georghiou, R. Morrow, and A.C. Metaxas. two-dimensional simulation of streamers

using the FE-FCT algorithm. *J. Phys. D: Appl. Phys.*, 33:L27–L32, 2000.

[12] A.A. Kulikovsky. The role of photoionization in positive streamer dynamics. *J. Phys. D: Appl. Phys.*, 33:1514–1524, 2000.

[13] R. Morrow and T.R. Blackburn. The stepped nature of lightning, and the upward connecting streamer. *J. Phys. D: Appl. Phys.*, 35:L69–L73, 2002.

[14] S.I. Braginskii. *Reviews of Plasma Physics*, volume 1, chapter Transport Processes in a Plasma, pages 205–311. Consultants Bureau, New York, 1965.

[15] R.F. Fernsler, A.W. Ali, J.R. Greig, and I.M. Vitkovitsky. The NRL CHMAIR code: a disturbed sea level air chemistry code. NRL Memorandum Report 4110, Naval Research Laboratory, 1979.

[16] P.L.G. Ventzek, R.J. Hoekstra, and M.J. Kushner. Two-dimensional modeling of high plasma density inductively coupled sources for materials processing. *J. Vac. Sci. Technol. B*, 12(1):461–477, Jan 1994.

[17] E.S. Oran and J.P. Boris. *Numerical Simulation of Reactive Flow.* Elsevier, New York, first edition, 1987.

[18] D.F. Gordon, W.B. Mori, and T.M. Jr. Antonsen. A ponderomotive guiding center particle-in-cell code for efficient modeling of laser plasma interactions. *IEEE Trans. Plasma Sci.*, 28(4):1224–1232, Aug 2000.

[19] S. Slinker and A.W. Ali. Electron excitation and ionization rate coefficients for N_2, O_2, NO, N and O. NRL Memorandum Report 4756, Naval Research Laboratory, 1982.

[20] A. Ting, D.F. Gordon, E. Briscoe, J.R. Peñano, and P. Sprangle. Direct characterization of self-guided femtosecond laser filaments in air. *Appl. Opt.*, 44(8):1474–1479, March 2005.

Appendix: TurboWAVE Normalizations

Although this report is written in cgs units, SPARC is not. SPARC consists of modules built on the turboWAVE framework. This framework was originally designed to treat collisionless plasmas, and assumes a certain normalization scheme appropriate for such problems. Although this scheme is not as appropriate for a code like SPARC, it is adopted for the sake of keeping everything built on the framework consistent.

The unit of time is ω_p^{-1} where $\omega_p = 2.8 \times 10^{14}$ rad/s is the plasma frequency in fully ionized air. The unit of length is c/ω_p, where c is the speed of light. The unit of mass is the electronic mass, m, and the unit of charge is the electronic charge, $|e|$. The unit of density is $n_p = m\omega_p^2/4\pi e^2$. Note that this results in the peculiarity that the unit of particle number is $N_p = mc^3/4\pi\omega_p e^2$. To determine the value of a normalized quantity in either SI or gaussian units, multiply the normalized quantity by the value given in Table V. For the case of SI units, we define the permittivity of free space, $\epsilon_0 = 8.85 \times 10^{-12}$ F/m, and the impedance of free space, $\eta_0 = 377\ \Omega$.

TABLE V: Normalization

Quantity	Symbol	SI Unit	cgs Unit	Unit Value
Time		ω_p^{-1}	ω_p^{-1}	3.55 fs
Length		c/ω_p	c/ω_p	1.06 μm
Density	n_p	$\epsilon_0 m\omega_p^2/e^2$	$m\omega_p^2/4\pi e^2$	2.5×10^{19} cm^{-3}
Particle Number		$\epsilon_0 mc^3/\omega_p e^2$	$mc^3/4\pi\omega_p e^2$	3×10^7
Electric Field	E_p	$mc\omega_p/e$	$mc\omega_p/e$	4.81 GV/cm
Electric Potential		mc^2/e	mc^2/e	512 kV
Magnetic Field		$m\omega_p/e$	$mc\omega_p/e$	1590 T
Current Density	j_p	$n_p ec$	$n_p ec$	1.2×10^{11} A/cm^2
Charge Density		$n_p e$	$n_p e$	4 C/cm^3
Conductivity		j_p/E_p	j_p/E_p	2500 mho/m
				2.3×10^{13} s^{-1}
2-Body Coefficient		ω_p/n_p	ω_p/n_p	1.1×10^{-5} cm^3/s
3-Body Coefficient		ω_p/n_p^2	ω_p/n_p^2	4.5×10^{-25} cm^6/s
Mobility		c/E_p	c/E_p	6.2 cm^2/V·s
Energy		mc^2	mc^2	8.2×10^{-14} J
Energy Density		$mc^2 n_p$	$mc^2 n_p$	2.1 MJ/cm^3
Power		$mc^2\omega_p$	$mc^2\omega_p$	23 W
Power Density		$mc^2\omega_p n_p$	$mc^2\omega_p n_p$	5.77×10^{20} W/cm^3
Temperature		mc^2/k_B	mc^2/k_B	512 keV
				5.93×10^9 K
Fluence		$E_p^2/\eta_0\omega_p$	$cE_p^2/4\pi\omega_p$	220 J/cm^2
Intensity	I_p	E_p^2/η_0	$cE_p^2/4\pi$	6.1×10^{16} W/cm^2
Cross Section		$\omega_p/n_p c$	$\omega_p/n_p c$	3.76×10^{-16} cm^2